Blood Oxygen Saturation Estimation in Transilluminated Images of Skin Lesions

Brian D'Alessandro, Atam P. Dhawan, *Fellow, IEEE*

***Abstract*—Estimating the oxygen saturation of blood surrounding skin lesions is critical for the early detection of skin cancer and malignancy such as melanoma. Through multispectral transillumination of the skin, a set of images can be obtained which helps visualize areas of subsurface absorption due to chromophores such as melanin, hemoglobin, and deoxyhemoglobin. To relate pixel intensity in these images to spatially located absorption coefficient values, we develop a correction factor to Beer's law, estimated through a Monte Carlo simulation of light propagation in skin, which takes into account the specific geometry of our transillumination imaging apparatus. We then use this relation on the multispectral imaging set for chromophore separation and oxygen saturation estimation. The separation method is validated through Monte Carlo simulation, as well as on a skin phantom. Results show that subsurface oxygen saturation can be reasonably estimated with good implications for the reconstruction of 3D skin lesion volumes using transillumination towards early detection of malignancy.**

I. Introduction

SKIN cancer is the most common form of malignancy, but the survival rate can be very good if the cancer is detected, diagnosed, and treated early. A novel technique for the early detection of skin cancers such as melanoma utilizes the principles of optical imaging and transillumination of the skin to reveal subsurface skin features such as the depth of a skin lesion and the blood volume surrounding the lesion. The Nevoscope [1], a hand-held device designed to provide transillumination imaging of the skin, directs light into the skin at a 45 degree angle through a fiber optic ring placed against the skin surface. Light diffuses through the skin tissue, and the photons which scatter back through the lesion up to the surface are captured by a CCD attached to the Nevoscope [see Fig. 1]. Since surface illumination is also blocked, the geometry of this illumination device essentially creates a virtual light source behind the skin lesion, thus providing a transilluminated image which contains important subsurface features for the early detection of skin cancer. By filtering the light source, a multispectral image set of the lesion can also be easily obtained.

One challenge associated with this method of imaging skin lesions is accurately measuring the subsurface skin features, in particular the spatially dependent absorption coefficient of objects within the skin. As a step toward that goal, in this paper we present a correction factor to Beer's law for light transmission through a medium which is tailored to the geometry of the Nevoscope device. The correction factor is developed by use of a Monte Carlo simulation of light propagation from the Nevoscope ring through the skin. We then use the corrected equation, along with the multispectral imaging set, to estimate the relative concentration of oxyhemoglobin and deoxyhemoglobin in an object embedded in the skin, first using simulated images and later using real images with the Nevoscope and a skin phantom.

Manuscript received October 14, 2011.

Brian D'Alessandro (email: bmd5@njit.edu) and Atam P. Dhawan (email: dhawan@njit.edu) are with the Department of Electrical and Computer Engineering, New Jersey Institute of Technology, Newark, NJ 07102 USA.

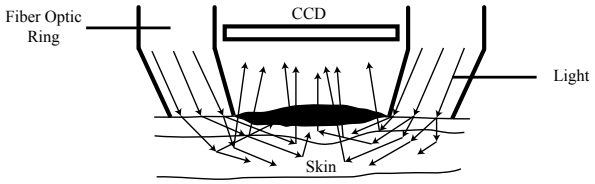

Fig. 1. Nevoscope Geometry

II. Methods

A. Beer's Law

As light propagates through a turbid medium such as the skin, the intensity of the light decreases due to absorption and scattering interactions with the medium. The extent of these interactions are characterized by the absorption and scattering coefficients, μ_a and μ_s. At the simplest level, the absorption coefficient μ_a is related to a change in light intensity by the Beer–Lambert law (or Beer's law), which states that for light transmitted through a medium over a path length of ℓ,

$$I/I_0 = e^{-\mu_a \ell} \tag{1}$$

where the incident light intensity is I_0, and the transmitted light intensity is I.

Because Beer's law only takes into account attenuated effects of absorption, but not scattering, many attempts have been made to introduce and quantify the scattering corrections needed for Beer's law [2], [3]. Such corrections can be mathematically complex, through reliance on solutions to the radiative transfer equation or other modeling. For highly scattering media, such as biological tissue, the diffusion equation is often used as an approximation of the radiative transport equation, where the dominant term in its solution for a semi-infinite slab is approximated by [4]–[6]:

$$\Phi(\ell) \sim C \cdot e^{-\mu_{\text{eff}} \ell} \tag{2}$$

where $\Phi(\ell)$ is the fluence rate, C is a constant and

$$\mu_{\text{eff}} \approx \sqrt{3\mu_a[\mu_a + (1-g)\mu_s]} \quad \text{if } \mu_a \ll \mu_s \tag{3}$$

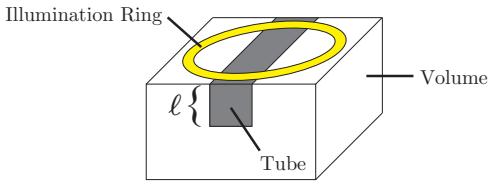

Fig. 2. Rectangular tube of depth ℓ embedded in a voxel grid volume.

Hence, an approximate scattering-corrected equation to Beer's Law may be written as:

$$I/I_0 = e^{-\mu_{\text{eff}}\ell} \tag{4}$$

In the Nevoscope geometry for skin lesion imaging, the angled fiber optic ring creates a virtual light source behind the lesion itself. Therefore, in (1) and (4), the light intensity I is the intensity value which is directly read by the CCD detector, and can thus be likened to the image pixel value at each pixel location. Similarly, the incident light intensity I_0 may be represented by an image of skin background, or, the transilluminated light without any lesion absorption interference. In this image-based representation, the relevant equation variables I, I_0, μ_a, and ℓ are all functions of pixel location (x, y).

We define the "true" relationship between the background corrected image I/I_0 and μ_a as an unknown function f:

$$I/I_0 = f\left(\ell, \mu_a, \mu_s\right) \tag{5}$$

The shape of this function can be observed through simulation using a voxel based Monte Carlo simulation of light propagation [7], [8]. In this simulation, individual photons of light are stepped through a virtual tissue volume whose voxels have their own independent set of optical properties. The simulation keeps track of photon position, direction, intensity, as well as the absorption, scattering, and internal reflection events which occur within the volume as the photon travels from voxel to voxel. If a photon is backscattered through the surface of the volume and hits a virtual detector grid, the photon intensity is recorded. Upon completion of many millions of simulated photons, this detector grid holds an image analogous to what would be recorded with the Nevoscope's CCD camera.

Hence, to find the true relationship of I/I_0 versus μ_a for an object embedded in skin, a small rectangular "tube" was defined within a 24×24×100 virtual voxel grid, representing a physical size of 1.2×1.2×0.5 cm^3. The embedded tube, with a width of 1 mm and a varying depth of ℓ, was defined in the uppermost layers of the volume [see Fig. 2]. The surface detector was defined to be a 7×7 grid, with each pixel of size 0.7 mm^2. The absorption coefficient of this tube was then set to increasing values, spanning μ_a = 0 cm^{-1} to 50 cm^{-1}. Other optical properties of the volume were set such that the simulation corresponded to imaging at 780 nm. For each value of μ_a in the tube, the simulation produced an image I, from which the average intensity value was computed over pixels within the tube ROI. Multiple simulations were also

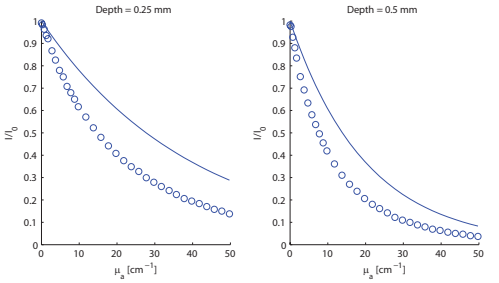

(a) True I/I_0 vs. μ_a (circles) compared with (1) (line).

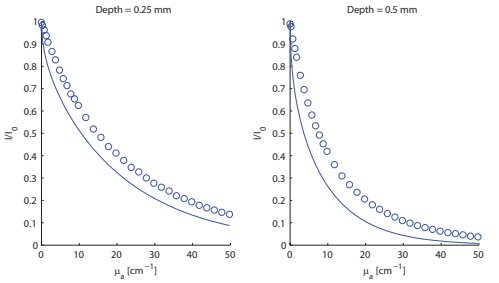

(b) True I/I_0 vs. μ_a (circles) compared with (4) (line).

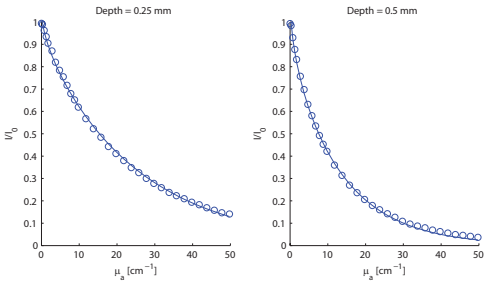

(c) True I/I_0 vs. μ_a (circles) compared with (8) (line).

Fig. 3.

run for varying depths of the tube, spanning $\ell = 0.25$ mm to 2 mm. The results of these simulations and the scatter plots of I/I_0 versus μ_a are visualized as circles in the graphs of Fig. 3. Only plots for tube depths of 0.25 mm and 0.5 mm are shown in the figure.

These simulated data points are compared to the predicted values produced by (1) in Fig. 3a, as well as (4) in Fig. 3b. In each plot, the solid line represents the predicted curve given by the equations while the plotted circles represent measurements from the Monte Carlo simulation.

B. Beer's Law with Nevoscope Geometry Correction

As is evident from Figs. 3a and 3b, there exists a clear discrepancy between simulated observation and mathematical approximation. Use of the scattering correction provided by (4) improves the match compared to (1) alone. Furthermore, (4) matches better for small depths, but the discrepancy between the approximated equation and reality increases as the object extends deeper.

It is not surprising that these discrepancies exist, because the geometry of illumination using the Nevoscope is not straight transmission, as Beer's law is designed for. While

the Nevoscope is said to create a virtual light source behind the lesion, the actual path of light is U-shaped, originating from the fiber optic ring, passing down through the skin and the lesion, and finally back up to the surface.

To compensate for this geometric characteristic, we introduce a correction factor R to (4) such that:

$$f\left(\ell, \mu_a, \mu_s\right) \sim e^{-\mu_{\text{eff}}\ell} \cdot e^{-\ell R} \tag{6}$$

Simulation and surface fitting was performed to estimate this μ_a- and depth-dependent correction factor R. The correction factor which provided an optimal fit between the observed data and corrected equation was given by:

$$R = -\left(4.5(\mu_a)^{0.18}\ell^{0.031} + 6.2\mu_a\ell\right) \tag{7}$$

Hence,

$$\begin{aligned} I/I_0 &= \exp\left(-\ell\sqrt{3\mu_a[\mu_a + (1-g)\mu_s]}\right) \\ &\quad \cdot \exp\left(4.5(\mu_a)^{0.18}\ell^{1.031} + 6.2\mu_a\ell^2\right) \end{aligned} \tag{8}$$

Comparison between the observed simulated data points and this new corrected equation are visualized in Fig. 3c. Naturally, the equation plot is designed to fit the data well, and this is the case over a large range of object depths ℓ.

C. Chromophore Separation

Given the good correction factor which allows for a corrected Beer's law equation specific to the Nevoscope illumination geometry, we wish to utilize (8) for the estimation of the unknown relative amounts of chromophores in the skin. In this situation, μ_a must first be estimated at each pixel location given I/I_0 and an estimate of ℓ. Hence, we find a spatially dependent image map of μ_a by inverting (5), where f is approximated by (8) to find:

$$\mu_a = f^{-1}\left(\ell, I/I_0, \mu_s\right) \tag{9}$$

This process is performed on each image obtained in the multispectral imaging set to find $\mu_a(\lambda)$, the absorption image map at wavelength λ. Subsequently, multiple linear regression can be performed on the linear mixing model:

$$\begin{aligned} \mu_a(\lambda) &= [\text{Mel}]\mu_a^{\text{Mel}}(\lambda) + [\text{HbO}_2]\mu_a^{\text{HbO}_2}(\lambda) \\ &\quad + [\text{Hb}]\mu_a^{\text{Hb}}(\lambda) \end{aligned} \tag{10}$$

to find [Mel], [HbO_2], and [Hb] (the unknown amounts of melanin, oxyhemoglobin, and deoxyhemoglobin respectively), where $\mu_a^{\text{Mel}}(\lambda)$, $\mu_a^{\text{HbO}_2}(\lambda)$, and $\mu_a^{\text{Hb}}(\lambda)$ are the known wavelength dependent absorption coefficients of melanin, HbO_2, and Hb.

III. Results

A. Monte Carlo Simulation

To test the ability of (8) to assist in the estimation of chromophore amounts in the skin, a simulation was devised whereby the same virtual volume and tube setup as described earlier was used. In this case, the depth of the tube was set to ℓ=1 mm, and the absorption coefficient of the tube was set such that the tube contained a mixture of HbO_2 and Hb. Multispectral imaging simulations were performed at 680 nm and 780 nm, and the system of equations for the linear mixing model was solved for the unknown amounts [HbO_2] and [Hb], while [Mel] was assumed to be zero. This unmixing procedure was performed using each of the three discussed methods of relating detector intensity to absorption coefficient for comparison. Oxygen saturation of the blood was defined as [SO_2]=[HbO_2]/([HbO_2]+[Hb]) and the results are shown in Fig. 4, relating the estimated [SO_2] fraction to the true [SO_2] fraction. In each plot, the solid line represents the ideal case where the estimated fraction equals the true fraction.

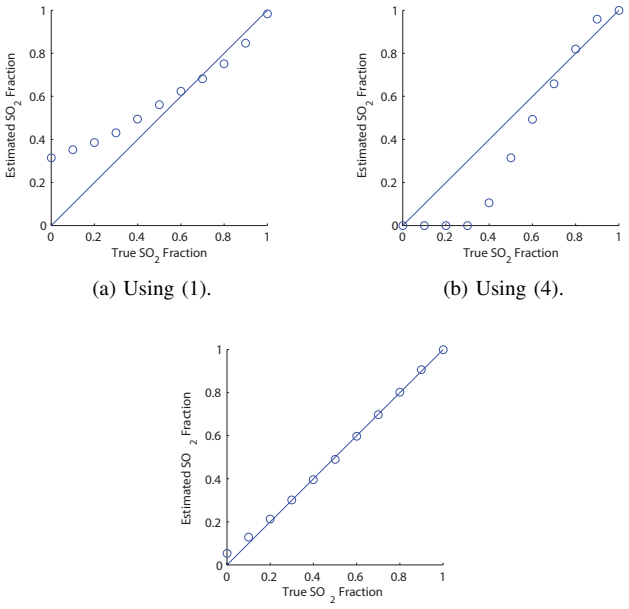

(a) Using (1). (b) Using (4).

(c) Using (8).

Fig. 4. Chromophore separation of [HbO_2] and [Hb] using the various equations for ℓ=1 mm.

While unmixing using (1) in Fig. 4a, as well as (4) in Fig. 4b show large errors especially towards situations with low oxygen saturation, the corrected method using (8) in Fig. 4c produces unmixing which is nearly linear, showing accurate estimation of the unknown [SO_2] fraction in a simulated environment for the entire range of possible [SO_2] values.

B. Skin Phantom

While chromophore separation was successful using Monte Carlo simulation, it was also desired to test the method in the real world using the actual Nevoscope. To do so, we used the Nevoscope to image a skin phantom containing an embedded circular capillary tube of inside diameter 1.15 mm, whose center was situated 0.575 mm below the surface. The skin phantom was created in a petri dish out of silicone, aluminum oxide particles, and cosmetic powder, and was designed to very closely match the optical properties of real skin in the visible and NIR range [9]. The capillary tube was filled with varying fractions of artificial HbO_2 and Hb (red and blue

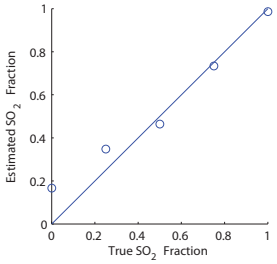

Fig. 5. Skin phantom chromophore separation graph

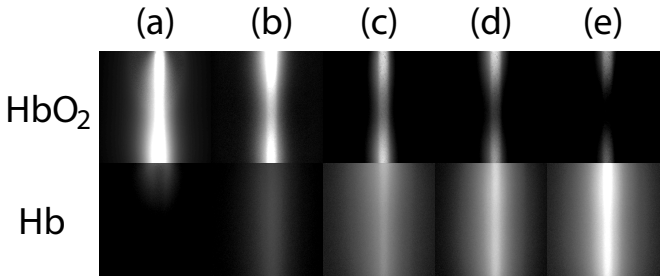

Fig. 6. Skin phantom chromophore separation images for (a) 100% HbO_2 & 0% Hb; (b) 75% HbO_2 & 25% Hb; (c) 50% HbO_2 & 50% Hb; (d) 25% HbO_2 & 75% Hb; (e) 0% HbO_2 & 100% Hb

food coloring). The optical absorption coefficients of these artificial substitutes were measured experimentally using a single integrating sphere. Imaging was performed using 600 nm and 875 nm transillumination imaging. Equation (8) was used with $\ell = 0.903$ mm, representing the average depth of the circular tube.

The plot of estimated $[SO_2]$ fraction to the true $[SO_2]$ fraction is presented in Fig. 5, while the resulting image estimates of $[HbO_2]$ and [Hb] are presented in Fig. 6. It is clear that the relative oxygen saturation ratio can reasonably be estimated from multispectral imaging and the corrected Beer's law equation, even for real world imaging using the actual imaging apparatus and a skin phantom. The accuracy is best for high levels of $[SO_2]$, while the accuracy decreases somewhat as $[SO_2]$ is reduced to zero. In practical application, $[SO_2]$ in human blood is usually around 75%, so it is encouraging to see the better accuracy in the most important range. The unmixing results prove the applicability of the corrected equation outside of simulation with potential applications in 3D reconstruction of skin lesions.

As a preliminary test to that end, 3D reconstruction was performed on a benign skin lesion, imaged using the Nevoscope at a dermatology clinic. Multispectral images were obtained at 600, 680, and 780 nm. The genetic algorithm (GA) based 3D reconstruction algorithm has been described in [8]. Initialization of the GA was done by random initialization, as well as through the use of (8) and the resulting 3D reconstructions are shown in Fig. 7. While validation is still ongoing for clinical lesions, use of the corrected equation to initialize the GA in this example produces a shallower reconstructed profile with less blood than the previously used

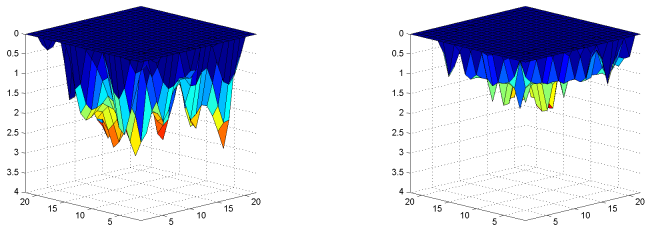

(a) Random GA initialization. (b) GA initialization using (8).

Fig. 7. Melanin & blood layer 3D reconstructed profile of a real benign skin lesion.

method of random initialization, fitting the fact that the lesion is benign.

IV. Conclusion

In conclusion, we have presented a method of relating the pixel intensity values in multispectral transilluminated images to the physical absorption coefficient values at that same location in the skin. This relation is defined through a correction factor to Beer's law for light transmission through a medium. By using this relation, the multispectral transilluminated images can be converted into absorption maps and by solving the system of equations for the mixing model of chromophores in the skin, an estimate of the relative amounts of each chromophore can be recovered. In so doing, the oxygen saturation level of blood within the skin can also be estimated. By evaluating this method on a skin phantom with embedded capillary tubes filled with artificial HbO_2 and Hb, the potential for oxygen saturation estimation is validated. In the future, we wish to refine integration of this method with the 3D skin lesion reconstruction algorithm with clinical validation.

References

[1] A. P. Dhawan, "Apparatus and method for skin lesion examination," U.S. Patent 5,146,923, September 15, 1992.

[2] W. G. Tam and A. Zardecki, "Multiple scattering corrections to the beer-lambert law. 1: Open detector," *Appl. Opt.*, vol. 21, no. 13, pp. 2405–2412, Jul 1982.

[3] L. Wind and W. W. Szymanski, "Quantification of scattering corrections to the beer-lambert law for transmittance measurements in turbid media," *Measurement Science and Technology*, vol. 13, no. 3, p. 270, 2002.

[4] W. Cheong, S. Prahl, and A. Welch, "A review of the optical properties of biological tissues," *Quantum Electronics, IEEE Journal of*, vol. 26, no. 12, pp. 2166 –2185, dec 1990.

[5] A. Ishimaru, *Wave Propagation and Scattering in Random Media*. New York: IEEE Press, 1999.

[6] S. A. Prahl, "Light transport in tissue," Ph.D. dissertation, The University of Texas at Austin, December 1988.

[7] L. Wang and S. L. Jacques, *Monte Carlo Modeling of Light Transport in Multi-layered Tissues in Standard C*. University of Texas, M.D. Anderson Cancer Centre, 1992.

[8] B. D'Alessandro and A. Dhawan, "Voxel-based, parallel simulation of light in skin tissue for the reconstruction of subsurface skin lesion volumes," in *Engineering in Medicine and Biology Society (EMBC), 2011 Annual International Conference of the IEEE*, 2011, pp. 8448–8451.

[9] M. Lualdi, A. Colombo, B. Farina, S. Tomatis, and R. Marchesini, "A phantom with tissue-like optical properties in the visible and near infrared for use in photomedicine," *Lasers in Surgery and Medicine*, vol. 28, no. 3, pp. 237–243, 2001.